Monthly Notices of the ROYAL ASTRONOMICAL SOCIETY

MNRAS **543,** 1214–1223 (2025) https://doi.org/10.1093/mnras/staf1533
Advance Access publication 2025 September 13

Impact of pulsar kicks on the evolution of supernova remnant-confined pulsar wind nebulae: axisymmetric RMHD modelling

Hongyu Wang, Qi Xia and Jun Fang ★
Department of Astronomy, Yunnan University, Kunming 650091, China

Accepted 2025 September 11. Received 2025 September 8; in original form 2025 July 15

ABSTRACT

This study uses 2.5-dimensional relativistic magnetohydrodynamic simulations to investigate the effects of a pulsar's high-velocity motion and the ambient medium density on the early-stage evolution of its pulsar wind nebulae (PWNe). Our results demonstrate that the velocity of the pulsar can significantly produce morphological asymmetry of the PWN, leading to significant off-centre displacement and distortion within the host supernova remnant. Moreover, a higher density of the interstellar medium intensifies and advances the interaction between the PWN and the reverse shock, resulting in stronger compression and enhanced synchrotron emission. The simulated radiative features, including offset toroidal structures and fragmented emission patches, show agreement with the asymmetric morphologies observed in several young PWNe, such as G327.1−1.1 and MSH 15−52. This work provides a compelling explanation for the morphological diversity among young PWNe and underscores the need for comprehensive three-dimensional simulations to capture more complex physical processes in future studies.

Key words: MHD – radiation mechanisms: non-thermal – methods: numerical – pulsars: general – ISM: supernova remnants.

1 INTRODUCTION

Massive stars undergo supernova explosions at the end of their life cycles. Following such an event, the stellar core may undergo gravitational collapse, resulting in the formation of a compact neutron star. Neutron stars characterized by rapid rotation and intense magnetic fields are known as pulsars. Through the release of rotational and magnetic energy, pulsars generate ultrarelativistic outflows, referred to as pulsar winds. When these pulsar winds interact with the surrounding medium – such as the interstellar medium (ISM) or supernova remnant (SNR) – they give rise to a bubble-like structure composed primarily of relativistic particles and magnetic fields, known as a pulsar wind nebula (PWN).

To date, more than 100 PWNe have been identified within the Milky Way. These objects rank among the brightest high-energy astrophysical sources in the Galaxy, with emission spanning a broad spectral range from radio wavelengths to hundreds of TeV and, in exceptional cases, reaching the PeV regime (Gaensler & Slane 2006; Zhu, Zhang & Fang 2018; Wu et al. 2023; Cao et al. 2024; Zhou et al. 2024). Typically, the radiation from radio to X-ray bands is dominated by synchrotron emission, whereas higher energy γ-rays are primarily attributed to the inverse Compton scattering process.

When pulsars are formed in supernova explosions, they generally impart a kick velocity because of the asymmetry of the explosion. This velocity spans a wide range, from as low as 10 km s^{-1} to as high as 1500 km s^{-1}, with a typical value of approximately 500 km s^{-1} (Pavan et al. 2016; Verbunt, Igoshev & Cator 2017). This velocity dictates the two primary evolutionary paths and morphologies of PWNe. In the early stages, the pulsar and its PWN are confined within the expanding ejecta of the parent SNR, the Crab Nebula serving as an archetypal example (Hester 2008). As the system evolves, the high-velocity pulsar eventually emerges from the SNR shell and travels supersonically through the ISM. At this point, the ram pressure balance between the pulsar wind and the ambient ISM forms a cometary structure with a distinct head and tail, known as a bow shock pulsar wind nebula (BSPWN; Wilkin 1996; Bucciantini 2018). Consequently, theoretical and simulation studies of PWNe have naturally diverged into two main branches, each focused on one of these distinct phases.

Substantial progress in the study of PWNe, particularly their intricate internal structures, has been driven by high-resolution observations, most notably from the *Chandra X-ray Observatory*. The iconic jet–torus structure revealed observationally in the Crab Nebula (Hester et al. 2002) directly challenged the early one-dimensional theoretical models (Kennel & Coroniti 1984). In response, two-dimensional (2D) axisymmetric relativistic magnetohydrodynamic (RMHD) simulations were developed. These models successfully demonstrated that an anisotropic pulsar wind can naturally form the observed jet–torus morphology via magnetic collimation (Komissarov & Lyubarsky 2003; Del Zanna, Amato & Bucciantini 2004; Del Zanna et al. 2006; Camus et al. 2009), and also reproduced other classical features of the Crab Nebula, such as wisps and knots (Helfand, Gotthelf & Halpern 2001; Gaensler et al. 2002; Lu et al. 2002; Romani & Ng 2003; Camilo et al. 2004; Slane et al. 2004; Romani et al. 2005). Subsequent research has progressed to full three-dimensional (3D) simulations to investigate the more complex dynamical processes driven by non-axisymmetric instabilities (Porth, Komissarov & Keppens 2013, 2014; Olmi et al. 2016). More recently, studies have begun to place PWNe within their broader evolutionary

★ E-mail: fangjun@ynu.edu.cn

context, incorporating their complex interactions with the host SNR and the influence of the circumstellar medium (CSM) shaped by the winds of the massive progenitor star (Meyer, Petrov & Pohl 2020; Meyer & Meliani 2022). However, these sophisticated models focusing on the internal dynamics of PWNe have, for the most part, assumed a stationary or slowly moving pulsar.

In parallel, significant progress has been made in the study of BSPWN during its later evolutionary phases. Early analytical and semi-analytical models laid the foundation for understanding the formation of bow shocks (Wilkin 1996). Subsequent numerical simulations have progressed in complexity: from initial 2D purely hydrodynamic simulations (Bucciantini 2002) to 2D RMHD simulations that incorporated magnetic fields (Toropina et al. 2001; van der Swaluw, Downes & Keegan 2004; Bucciantini, Amato & Del Zanna 2005), and ultimately to 3D magnetohydrodynamic (MHD)/RMHD simulations capable of addressing the general case where the pulsar's spin axis is misaligned with its velocity vector (Vigelius et al. 2007; Barkov, Lyutikov & Khangulyan 2019). These studies have investigated in detail how factors such as the anisotropy and magnetization of the pulsar wind, as well as its interaction with the ISM, for instance, the inhomogeneity or ionization state of the medium (Olmi, Bucciantini & Morlino 2018; Olmi & Bucciantini 2019; Toropina, Romanova & Lovelace 2019; Xia et al. 2025), shape the diverse morphologies observed in BSPWNe. Collectively, this work constitutes our primary understanding of the long-term evolution of pulsars after they escape their parent SNR.

In summary, current numerical simulation research has achieved significant success in two mature but relatively distinct domains. However, the complex dynamics of the crucial transitional phase connecting these two stages – namely, the early evolution of a pulsar with a significant kick velocity while it is still embedded within its SNR – remain a critical yet underexplored area of research. During this phase, there is a vigorous and continuously evolving interaction between the high-velocity pulsar, its associated PWN, and the surrounding, coexpanding SNR ejecta. Some prior work has addressed the modelling of moving pulsars inside SNRs (Blondin, Chevalier & Frierson 2001; van der Swaluw et al. 2003, 2004; Temim et al. 2015, 2017). More recently, Meyer, Torres & Meliani (2025) have significantly advanced this line of research by incorporating the systematic effects of both the progenitor's stellar wind and the pulsar's velocity. Studies have shown that the asymmetric CSM left by the progenitor star, particularly its dense bow shock, can act as a dynamical obstacle, significantly deflecting the high-velocity pulsar jet by approximately 40–50°. This mechanism provides a direct and natural physical explanation for the observed north–south asymmetric tails in young pulsars, such as PSR J1509−5850. It is precisely because the complex coupling effects between the CSM and the kick velocity have already been successfully modelled by Meyer's team that our pure kick model is established as an indispensable benchmark. Therefore, the objective of this paper is to systematically investigate the influence of the pulsar's kick velocity and varying uniform ISM densities on the early coevolution of the PWN–SNR composite system, employing high-resolution 2.5-dimensional (2.5D) RMHD numerical simulations. This research is crucial for explaining the observed diversity in young PWNe, such as their positional offsets, morphological distortions, and asymmetric brightness distributions.

The structure of the paper is as follows. In Section 2, we introduce the numerical modelling framework. Section 3 presents the simulation results obtained under various model parameters. Finally, in Section 4, we compare the simulation results with observational data, thereby validating our results and providing better explanations of the observed characteristics of PWNe.

2 PHYSICAL AND NUMERICAL MODEL

2.1 Governing equations and pulsar wind model

This work utilizes the ATHENA++ code to numerically simulate the RMHD equations. We adopt the conservative formulation within the relativistic framework from Stone et al. (2020), which governs the conservation of mass, momentum, energy, and magnetic flux. The equations are as follows:

$$\frac{\partial D}{\partial t} + \nabla \cdot (D\boldsymbol{v}) = 0, \tag{1a}$$

$$\frac{\partial \boldsymbol{M}}{\partial t} + \nabla \cdot \boldsymbol{S} = 0, \tag{1b}$$

$$\frac{\partial E}{\partial t} + \nabla \cdot \boldsymbol{M} = 0, \tag{1c}$$

$$\frac{\partial \boldsymbol{B}}{\partial t} - \nabla \times (\boldsymbol{v} \times \boldsymbol{B}) = 0. \tag{1d}$$

The conserved variables involved here are the laboratory-frame density (D), energy (E), momentum ($\boldsymbol{M}$), and the stress tensor ($\boldsymbol{S}$), which are defined as follows:

$$D = \gamma\rho, \tag{2a}$$

$$E = \gamma^2 w - \gamma^2(\boldsymbol{v}\cdot\boldsymbol{B})^2 - (p_{\rm g} + p_{\rm m}), \tag{2b}$$

$$\boldsymbol{M} = (E + p_{\rm g} + p_{\rm m})\boldsymbol{v} - (\boldsymbol{v}\cdot\boldsymbol{B})\boldsymbol{B}, \tag{2c}$$

$$\boldsymbol{S} = \gamma^2 w\boldsymbol{v}\boldsymbol{v} - \frac{1}{\gamma^2}\boldsymbol{B}\boldsymbol{B} - (\boldsymbol{v}\cdot\boldsymbol{B})(\boldsymbol{v}\boldsymbol{B} + \boldsymbol{B}\boldsymbol{v}) - \gamma^2(\boldsymbol{v}\cdot\boldsymbol{B})^2\boldsymbol{v}\boldsymbol{v} + (p_{\rm g} + p_{\rm m})\boldsymbol{I}. \tag{2d}$$

Here, ρ, $P_{\rm g}$, and $P_{\rm m}$ are the appropriate density, gas pressure, and magnetic pressure, respectively. The variable $\boldsymbol{u}$ denotes the spatial component of the four-velocity fluid of the laboratory frame, and $\boldsymbol{B}$ is the four-vector magnetic field in the laboratory frame. The three-velocity is given by $\boldsymbol{v} = \boldsymbol{u}/\gamma$, where γ is the Lorentz factor. The total enthalpy w can be expressed as

$$w = \rho + \frac{\Gamma}{\Gamma - 1}p_{\rm g} + 2p_{\rm m}, \tag{3}$$

where Γ is the adiabatic index, which is assumed to be constant. Our model adopts an ideal gas equation of state with an adiabatic index $\Gamma = 4/3$.

The pulsar wind, as a key physical factor that determines the morphology and structure of the PWN, is mainly governed by the latitudinal dependence of the energy flux in the unshocked pulsar wind, which follows a dependence $\sin^2\theta$ (Bogovalov & Khangoulyan 2002; Lyubarsky 2002). This angular dependence is related to the structure of the toroidal magnetic field, and in the split-monopole model of the pulsar magnetosphere (Michel 1973), it is assumed that the predicted energy flux depends on the inhomogeneous distribution characteristics in space, i.e. $F(r,\theta) \propto r^{-2}\sin^2\theta$. In order to extend the RMHD equations to the context of a pulsar wind, this study incorporates the assumption that the wind's energy flux possesses a spatially anisotropic distribution. The flux can be expressed as

$$\mathcal{F}(\theta) = \frac{\alpha + (1-\alpha)\sin^2\theta}{k}, \quad F(r,\theta) = \frac{L_0}{4\pi r^2}\mathcal{F}(\theta), \tag{4}$$

where $L_0 = 5 \times 10^{39}\,{\rm erg\,s^{-1}}$ represents the spin-down luminosity of the pulsar, $\alpha \ll 1$ is the anisotropy parameter that governs the ratio

between the polar and equatorial energy flux, and k is a normalization factor. The principle of energy conservation requires that

$$\int_0^{2\pi}\int_0^{\pi} F(r,\theta)r^2\sin\theta\,\mathrm{d}\theta\,\mathrm{d}\phi = L_0. \tag{5}$$

Substituting equation (4) into equation (5) and performing the integration, we obtain $k = 1-(1/3)(1-\alpha)$. Thus, the pulsar wind energy flux at any specific coordinate (r,θ) within the computational domain is defined as

$$F(r,\theta) = \frac{L_0}{4\pi r^2}\mathcal{F}(\theta), \quad \mathcal{F}(\theta) = \frac{\alpha+(1-\alpha)\sin^2\theta}{1-(1-\alpha)/3}. \tag{6}$$

The split-monopole model provides a reasonable approximation of the global magnetic field structure from the polar regions to the equator. However, it remains insufficient to capture the complex physical processes that occur in the equatorial region. Coroniti (1990) further proposed that the pulsar wind may exhibit a striped structure near the equator, where the dissipation between stripes leads to a decay in magnetic field strength. This requires a modification of the original model. Consequently, a function $G(\theta)$ is introduced, along with a parameter σ_0, to redefine the magnetic field strength. The resulting expression is given by

$$G(\theta) = \sin\theta\,\tanh\left[b\left(\frac{\pi}{2}-\theta\right)\right], \quad B(r,\theta) = \sqrt{\frac{\sigma_0 L_0}{c}}\frac{G(\theta)}{r}, \tag{7}$$

where σ_0 characterizes the magnitude of the magnetic field B, and typically ranges from 10^{-3} to 0.1 (Kennel & Coroniti 1984; Bucciantini et al. 2004; Del Zanna et al. 2006). The function $G(\theta)$ accounts for two factors: the latitude dependence($\sin\theta$) of the split magnetic monopoles and the expected striped structure ($\tanh[b((\pi/2)-\theta)]$) of the pulsar wind (Coroniti 1990). Regarding the configuration of model parameters, we adopt a magnetization parameter $\sigma_0 = 0.025$, an anisotropy parameter $\alpha = 0.1$, and a striped wind-related parameter $b = 10$. These values were chosen to effectively model the highly anisotropic pulsar wind in the vicinity of the equatorial plane of the magnetosphere.

The energy flux of the pulsar wind consists of both the kinetic energy flux of the particles and the magnetic energy flux; it can be expressed as

$$F(r,\theta) = \left(\frac{B(r,\theta)^2}{4\pi} + nm_\mathrm{e}c^2\gamma_0^2\right)c, \tag{8}$$

where n denotes the particle number density of the pulsar wind, m_e is the mass of the electron, γ_0 is the Lorentz factor of the pulsar wind, B represents the magnetic field strength, and c is the speed of light. By substituting equations (6) and (7) into equation (8) and performing the simplification, the particle number density can be expressed as

$$n(r,\theta) = \frac{L_0}{4\pi c^3 m_\mathrm{e}\gamma_0^2}\frac{1}{r^2}\left[\mathcal{F}(\theta)-\sigma_0 G^2(\theta)\right]. \tag{9}$$

The passive scalar is used to trace the pulsar wind material, where the scalar value Q follows the advection equation:

$$\frac{\partial(\rho Q)}{\partial t} + \nabla\cdot(\boldsymbol{v}\rho Q) = 0. \tag{10}$$

This tracer moves passively with the fluid, allowing us to identify the pulsar wind region. Within the pulsar wind material region, the value of Q is set to $Q(r) = 1$, while in other regions $Q(r) = 0$, where r denotes the position of a grid cell in the simulation domain.

2.2 Numerical set-up and initial conditions

We employ a 2.5D RMHD numerical simulation method to construct the computational model. The computational domain is discretized with 8192 grids in the radial direction r, ranging from 0.1 to 16.0 pc. The inner boundary utilizes a user-defined physical condition (see the formula in this section) to describe the injection of magnetized wind from a compact object. The outer boundary is set to a free-outflow condition to simulate the open characteristics of the ISM. In the polar direction (θ), 256 grids cover the angle range [0, π], and the polar wedge boundary treatment method effectively avoids numerical singularity issues at the pole of the spherical coordinate system. The azimuthal direction (ϕ) is simplified with a single-grid periodic boundary condition, reducing the 3D problem to a 2.5D model to balance computational efficiency. For high-accuracy computations of mixed shock–turbulence environments, we use the HLLD (Harten–Lax–van Leer discontinuities) Riemann solver with a third-order PPM (piecewise parabolic method) scheme to handle discontinuities, implement three ghost cell layers to ensure boundary data integrity and suppress numerical artefacts, and set the CFL (Courant–Friedrichs–Lewy) number at 0.3 for stability.

The initial conditions for the simulation domain are structured into four concentric, annular regions, distinguished by their physical properties (from outermost to innermost). The outermost region consists of a fully ionized ISM with a density of $n = 0.1$ or $0.5\,\mathrm{cm}^{-3}$. The second region contains cold supernova ejecta with a total mass of $M_\mathrm{ej} = 3\,\mathrm{M}_\odot$, which exhibit a radial expansion velocity profile of $v \propto r$. The third region represents a primordial bubble that is evolving and will subsequently merge with the PWN. The innermost region is composed of a cold magnetized pulsar wind injected at the inner boundary r_min, expanding with a relativistic Lorentz factor of $\gamma_0 = 100$. Although this value is significantly lower than that typical for the Crab pulsar wind (Kennel & Coroniti 1984), it remains sufficiently high to ensure that the flow is highly relativistic. In this regime, the post-shock dynamics are independent of the specific value of the Lorentz factor (Olmi et al. 2014).

Furthermore, to investigate the effect of the pulsar's proper motion on the dynamical evolution of the PWN, we adopt an equivalent velocity model via a reference frame transformation. This is implemented by imposing an initial velocity field $\boldsymbol{V}_\mathrm{ISM} = -\boldsymbol{V}_\mathrm{pulsar}$ on the ambient ISM.

This study assumes that the supernova ejecta expand into a uniform ISM. This is a simplification that neglects the complex circumstellar environment – such as wind-blown bubbles or dense circumstellar shells – that could be formed by the stellar winds of progenitor stars, such as Wolf–Rayet (WR) stars or red supergiants (RSG). The objective of this approach is to isolate the influence of the pulsar kick velocity, a key parameter, on the evolution of the PWN within the SNR. This avoids introducing additional free parameters and complexities associated with a progenitor environment. Such a methodology allows us to clearly disentangle and understand the effects of the pulsar motion itself. The potential impact of the progenitor wind on our results will be discussed in further detail in the Discussion section (Section 4.1).

2.3 Synchrotron emission modelling

In this work, to facilitate comparison with extensive observational data on synchrotron radiation from non-thermal particles in the PWN, we constructed a map of synchrotron surface brightness based on RMHD simulations. The synchrotron radiation spectrum of the PWN is assumed to be described by particles with a power-law distribution

Table 1. Simulation set-up parameters for the four models.

Model	$V_{\mathrm{pulsar}\,z}$ (km s^{-1})	n_{ISM} (cm^{-3})	Description
A	0	0.1	Stationary pulsar, low-density ISM
B	0	0.5	Stationary pulsar, high-density ISM
C	500	0.1	Moving pulsar, low-density ISM
D	500	0.5	Moving pulsar, high-density ISM

in energy, i.e.

$$N(E) = K E^{-s}, \tag{11}$$

where E denotes the electron energy. We adopt the non-thermal synchrotron radiation model from Meyer et al. (2021) and, following the theoretical framework for magnetized plasmas presented by Jun & Norman (1996), set the exponent $s = 2$ to represent a strong shock. Consequently, the synchrotron emissivity at a specific observation frequency ν can be expressed as

$$j_{\mathrm{sync}}(\nu) \propto K^{2-s}\, p^{s-1}\, B_{\perp}^{\frac{s+1}{2}}\, \nu^{-\frac{s-1}{2}}, \tag{12}$$

which reduces to

$$j_{\mathrm{sync}}(\nu) \propto p^{s-1}\, B_{\perp}^{\frac{s+1}{2}}\, \nu^{-\frac{s-1}{2}}. \tag{13}$$

Here p is the thermal pressure of the gas and $B_{\perp}$ denotes the component of the magnetic field perpendicular to the line of sight. Let the unit vector along the observer's line of sight be $\boldsymbol{l}$, and define the observer's viewing angle as $\theta_{\mathrm{obs}} = \angle(\boldsymbol{l}, \boldsymbol{B})$. Then, the perpendicular component of the magnetic field can be expressed as

$$B_{\perp} = |\boldsymbol{B}| \sin\left(\theta_{\mathrm{obs}}\right). \tag{14}$$

Furthermore, the projection of the magnetic field onto the normal plane to the observation plane can be quantified as

$$B_{\perp} = |\boldsymbol{B}| \sqrt{1 - \left(\frac{\boldsymbol{B}\cdot\boldsymbol{l}}{|\boldsymbol{B}|}\right)^2}. \tag{15}$$

Then, the emission coefficient is

$$j_{\mathrm{sync}} \propto p^{s-1} \left(|\boldsymbol{B}| \sqrt{1 - \left(\frac{\boldsymbol{B}\cdot\boldsymbol{l}}{|\boldsymbol{B}|}\right)^2}\right)^{\frac{s+1}{2}} \nu^{-\frac{s-1}{2}}. \tag{16}$$

In the simulated numerical box, the 2D data are rotated along the axis of symmetry to generate axisymmetric 3D data. The data are then interpolated from spherical coordinates to Cartesian coordinates. During the visualization stage, the astronomical analysis tool YT is used to integrate projections along the line of sight to obtain synchrotron surface brightness maps. This process can be represented by

$$I = \int j_{\mathrm{sync}}\left(\theta_{\mathrm{obs}}\right) \mathrm{d}l. \tag{17}$$

3 SIMULATION RESULTS

This section aims to investigate the influence of the pulsar's spatial velocity on the evolution of a confined PWN. Specifically, we examine the effects that arise from variations in the pulsar velocity and the density of the surrounding ISM. In our simulations, we consider two representative pulsar velocities: 0 km s^{-1}, corresponding to a stationary pulsar, and 500 km s^{-1}, representing a moving pulsar. Since the simulations are performed under the assumption of axisymmetry, the motion of the pulsar is restricted to the z direction.

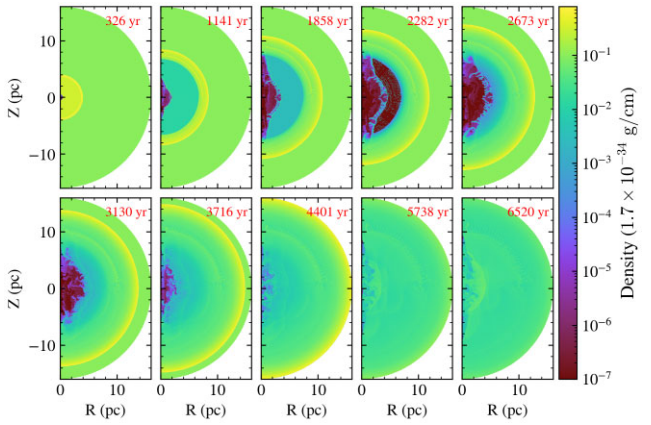

Figure 1. Density evolution of Model A (pulsar velocity = 0 km s^{-1}, n = 0.1 cm^{-3}) at 10 evolutionary stages: 326, 1141, 1858, 2282, 2673, 3130, 3716, 4401, 5738, and 6520 yr.

Consequently, the velocity components in the x and y directions are set to zero. That is, the pulsar velocity satisfies $V_{\mathrm{pulsar}} = V_{\mathrm{pulsar}\,z}$, with $V_{\mathrm{pulsar}\,x} = V_{\mathrm{pulsar}\,y} = 0$. In addition, the ISM density was set to two values: 0.1 and 0.5 cm^{-3}. These combinations result in four simulation scenarios, as shown in Table 1.

Within the standard framework of RMHD, our simulations yield a suite of fundamental primitive physical variables, including mass density, thermal pressure, and the three components of the magnetic field (B_r, B_θ, and B_ϕ). To more effectively illustrate the dynamical evolution of the PWN, and to reduce visual interference caused by the inherent bipolarity of magnetic field slices, particularly in the representation of vortex structures in evolutionary snapshots, we introduce an additional user-defined variable as a supplementary diagnostic quantity. This variable corresponds to the magnetic pressure (P_{mag}), which enhances our ability to capture the detailed interaction between the reverse shock and the PWN boundary. Magnetic pressure is computed as $P_{\mathrm{mag}} = 0.5\left(B_r^2 + B_\theta^2 + B_\phi^2\right)$.

3.1 PWN driven by a stationary pulsar

Figs 1 and 2 present the temporal evolution of the density slices for Model A and Model B, respectively. These sequences capture the dynamical evolution of the system from the onset of pulsar wind particle injection, spanning from year 326 to year 6520, and consist of 10 snapshots corresponding to key evolutionary stages. As shown in Fig. 1, by year 1141 after the onset of pulsar wind particle injection, the four characteristic structural regions described by the numerical model have become clearly distinguishable: (1) the innermost region corresponds to the PWN, formed by particle injection from the inner boundary; (2) surrounding the PWN is a low-density, thermally dominated bubble; (3) extending outward is a complex shock interaction region produced by the supernova explosion, which contains both the outward-propagating forward

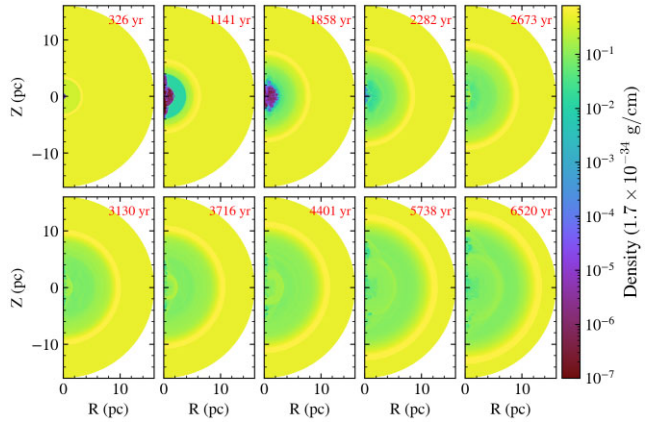

Figure 2. Density evolution of Model B (pulsar velocity = 0 km s^{-1}, $n = 0.5$ cm^{-3}).

shock and the reverse shock; and (4) the outermost region consists of the undisturbed, low-density ISM.

In the stationary pulsar evolution model (Model A), both the forward shock and the reverse shock of the SNR exhibit a centrally symmetric morphology. Meanwhile, the highly magnetized pulsar wind injected at 0.1 pc gives rise to axially symmetric, bipolar polar outflows along the z-axis. Figs 1 and 2 clearly demonstrate the full evolutionary sequence of the PWN, including its initial free expansion, compression due to interaction with the reverse shock, and subsequent re-expansion. However, in comparison to Model A, which assumes a low-density ISM environment, and Model B, which adopts a high-density ISM, exhibits the following notable differences: the interaction between the PWN and the reverse shock occurs at an earlier time; the duration of compression by the reverse shock is shorter; and the radial expansion of the forward shock is more strongly suppressed due to the higher ISM density.

3.2 PWN driven by a moving pulsar

Fig. 3 present the simulation results of Model C, showing the density slices. As illustrated in Fig. 3, in year 1141 after the onset of particle injection of the pulsar wind, the PWN produced by the moving pulsar exhibits a diamond-shaped morphology similar to that reported by Komissarov & Lyubarsky (2004), rather than the bipolar symmetric structure observed in the stationary pulsar case (Fig. 1).

By 1858, the polar regions of the PWN began to interact with the reverse shock of the SNR. As the dynamical evolution proceeds, the entire PWN enters the compression phase dominated by the reverse shock by year 2673. During this phase, the high-density supernova ejecta, driven by hydrodynamic compression, significantly altered the morphology of the PWN. By year 3130, due to the imposed motion of the pulsar along the positive z-axis,the compressive effects of the reverse shock become strongly asymmetric, characterized by a noticeable displacement of the main body of the PWN towards the negative z-direction. Subsequently, by year 4955, the energy accumulated during the shock interaction begins to be released, and the PWN enters a re-expansion phase. This complete evolutionary process is clearly confirmed in the density slice in year 5738, where a systematic outward expansion of the high-density material of the PWN is quantitatively observable within the spatial domain defined by a radial distance $R \in [0, 4]$ pc and a height $Z \in [-7, 0]$ pc.

Fig. 5 shows the $P_{\rm mag}$ evolution slices for Model C, the RMHD characteristics of the interaction between the PWN and the SNR

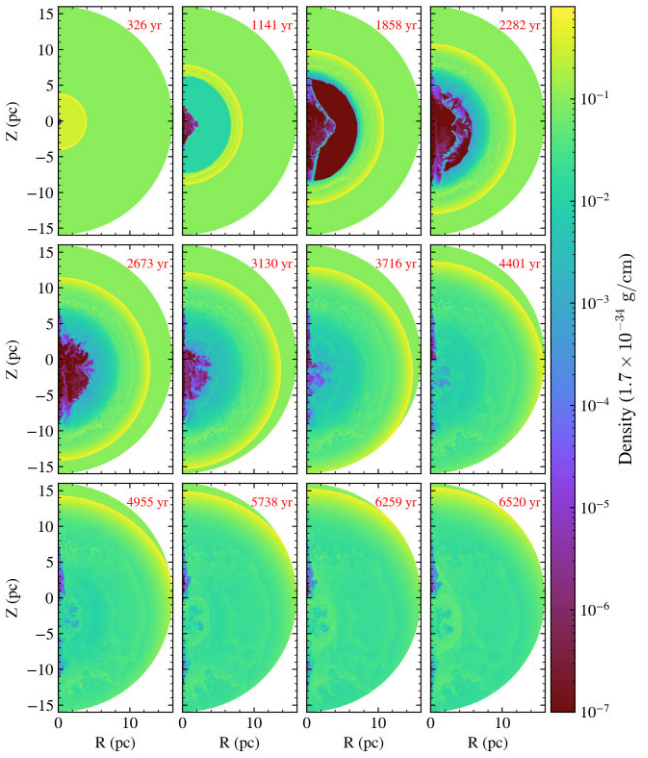

Figure 3. Density evolution of Model C (pulsar velocity = 500 km s^{-1}, $n = 0.1$ cm^{-3}) at 326, 1141, 1858, 2282, 2673, 3130, 3716, 4401, 4955, 5738, and 6520 yr, respectively.

are revealed more clearly compared to the density distribution. In 1858, the $P_{\rm mag}$ slice indicates the onset of weak Rayleigh–Taylor instabilities (RTIs) at the interface between the polar regions of the PWN and the reverse shock of the SNR. By year 2673, when the PWN becomes fully embedded within the reverse shock interaction zone, the $P_{\rm mag}$ distribution exhibits a prominent multilayered structure: a central region dominated by a freely expanding magnetized plasma, surrounded by a low magnetic field cavity with a thickness of approximately $\Delta r \approx 3$ pc, and an outermost thin shell characterized by RTI induced by the reverse shock. It should be noted that spatially selective enhancement of the RTI becomes particularly evident at this stage. Non-linear vortex structures develop predominantly in the polar regions, whereas only linear-phase shell perturbations are sustained near the equatorial plane ($Z \in [-5, 5]$ pc). Subsequently, by year 3130, continued compression by the reverse shock leads to the collapse of the central PWN magnetic confinement. The magnetic energy-dominated region undergoes a topological transition, resulting in the formation of a filamentary structure with fractal characteristics (Blondin et al. 2001). By year 4955, during the re-expansion phase of the PWN, it exhibits a distinct anisotropic expansion along the z-axis, with the negative extension reaching approximately 1.7 times the positive extension. This asymmetry is directly associated with Doppler-enhanced shock effects resulting from the pulsar velocity ($v_{\rm PSR} = 500$ km s^{-1}). Numerical analysis indicates a systematic contraction of the low-magnetic-field cavity volume during this stage.

Finally, by 6520, the SNR forward shock has propagated beyond the simulation boundary ($r \geq 16$ pc), and the PWN has developed a significant bipolar asymmetry along the z-axis, extending up to 10 pc in the positive direction and 15 pc in the negative direction. The overall dynamical evolution is concentrated within the lower

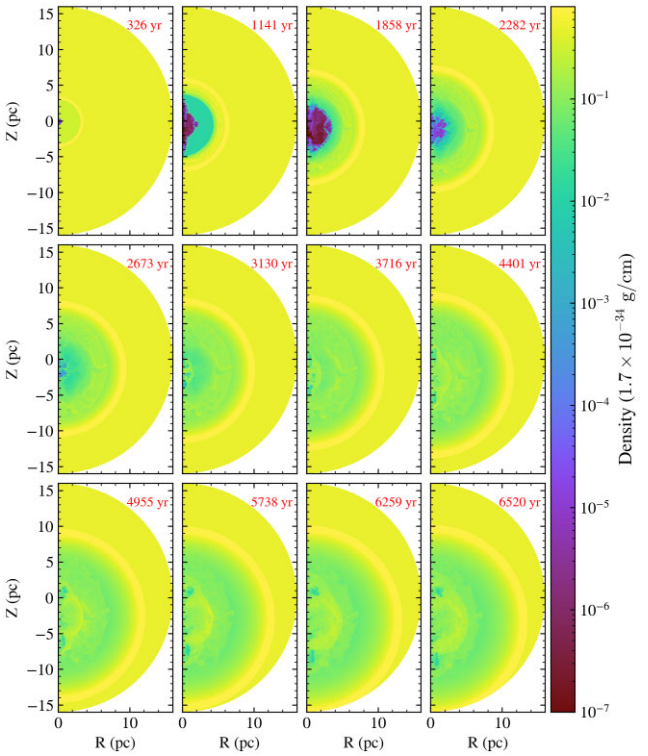

Figure 4. Density evolution of Model D (pulsar velocity = 500 km s^{-1}, $n = 0.5$ cm^{-3}).

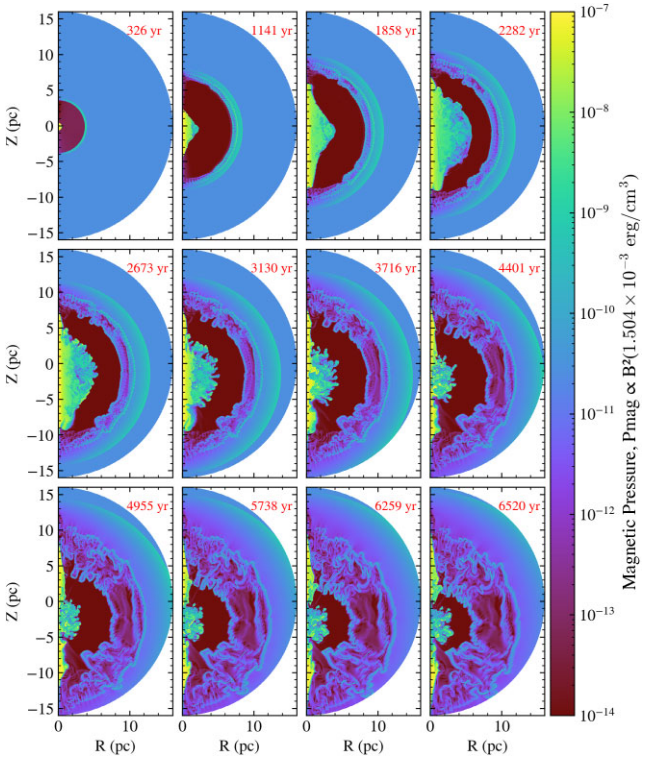

Figure 5. Magnetic pressure evolution in Model C (pulsar velocity = 500 km s^{-1}, $n = 0.1$ cm^{-3}).

hemisphere of the simulation domain, for which the spatial velocity of the pulsar provides a physically consistent explanation for the observed asymmetry. It is noteworthy that, for such a rapidly moving pulsar, the formation of a bow shock was not evident at the end of the simulation. This observation calls for additional study and discussion.

Figs 4 and 6 present the numerical simulation results for Model D, in which the pulsar is assigned an initial velocity of 500 km s^{-1} and the ambient ISM has a density of $n = 0.5$ cm^{-3}. Compared to the low-density medium case (Model C), the dynamical evolution of Model D exhibits a pronounced compression effect on the timescale. The outward expansion of the forward shock of the SNR is significantly inhibited. By as early as the year 1858, the freely expanding central PWN has already encountered the reverse shock, an interaction that does not occur until year 2673 in Model C. By year 2282, the reverse shock has compressed the PWN from a radius of 4 pc down to approximately 2 pc, with a compression rate several times higher than that observed in Model C. This strong compression phase lasts for approximately $\Delta t \approx 1200$ yr, until the system enters the re-expansion phase at year 3130.

As shown in the $P_{\rm mag}$ distribution for Model D in Fig. 6, the diamond-shaped structure of the central PWN, observed during its interaction with the reverse shock at 1858 years, becomes significantly deformed due to the high-density ISM environment. Meanwhile, the outer SNR shell has expanded radially to only about 8 pc, whereas, in the corresponding low-density model, the expansion reaches up to 12 pc at the same epoch. Although the overall morphology $P_{\rm mag}$ shares similarities with that of the lower density Model C, a key distinction arises after the PWN compression at year 2282. Fig. 6 shows that the RTI shell begins to exhibit perturbations specifically along the equatorial plane. By year 3716, at the onset of the re-expansion phase, the central high $P_{\rm mag}$ appears more diffuse

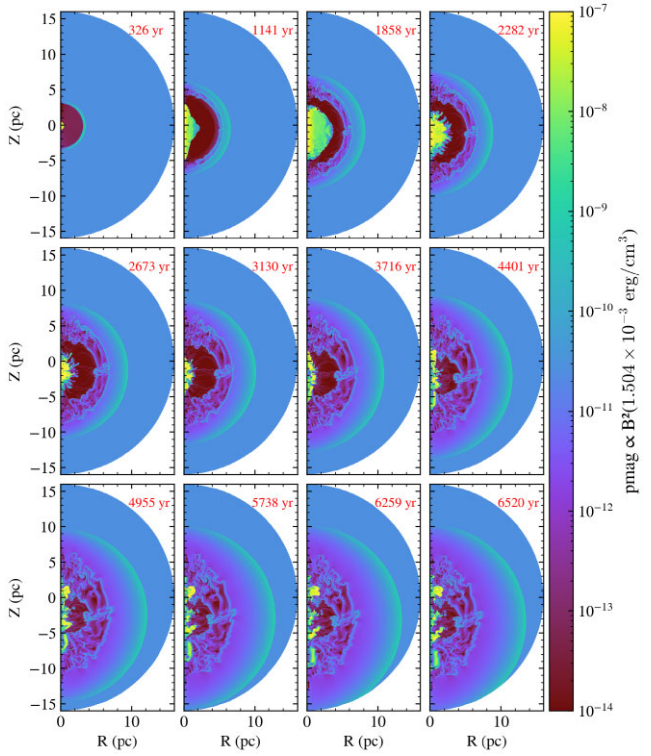

Figure 6. Magnetic pressure evolution in Model D (pulsar velocity = 500 km s^{-1}, $n = 0.5$ cm^{-3}).

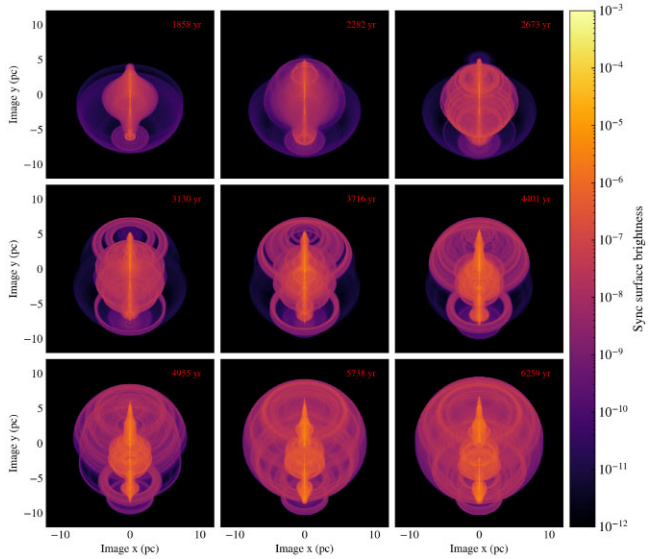

Figure 7. Synchrotron surface brightness distribution of Model C at a frequency of 2.4×10^{24} Hz, viewed along a 45° inclination angle relative to the symmetry axis.

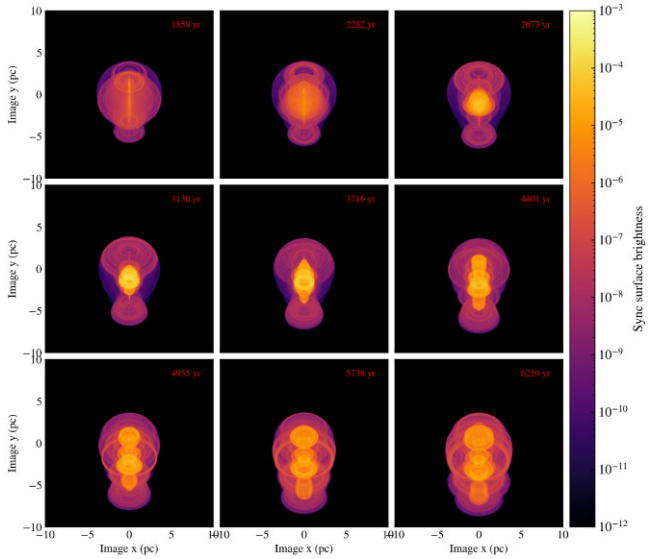

Figure 8. Synchrotron surface brightness distribution of Model D at a frequency of 2.4×10^{24} Hz, viewed along a 45° inclination angle relative to the symmetry axis.

in Model D compared to Model C. Furthermore, no prominent collimated jet-like features form along either direction of the z-axis, in contrast to the bipolar structures observed in the lower density case. Furthermore, although the high-density medium significantly compressed the temporal and spatial scales of the reverberation phase compared to the low-density ISM model, no bow shock structure was observed by the simulation's conclusion, a result similar to that of Model C.

3.3 Synchrotron emission surface brightness maps

In this study, we employ axisymmetric geometries and construct a 3D data set by applying rotational symmetry operations to high-resolution 2D simulation data. This approach effectively realizes a 2.5D numerical simulation framework analogous to that introduced by Meyer et al. (2021) and Meyer, Meliani & Torres (2024) in their investigations of radiative transfer in PWNe. A passive scalar field tracer technique is implemented within the RMHD framework: passive scalar tracers are injected from the inner boundary to kinetically track the motion of pulsar wind particles. The computational advantage of this method lies in the fact that 3D data reconstruction is applied only to the regions identified by the tracer as dynamically active PWN zones. Based on theoretically derived synchrotron emissivity distribution functions, we perform line-of-sight integration projections of the 3D emission volume using the YT visualization and analysis platform (Turk et al. 2011). This method differs from the RAMC3D radiative transfer scheme used by the Meyer group in their 2.5D simulations. The final product is the surface brightness distribution of synchrotron radiation projected onto a 3D observational plane. Figs 7 (Model C) and 8 (Model D) display the simulated synchrotron surface brightness maps of the PWN at a frequency of 2.4×10^{24} Hz. According to the calculation in Section 2.3, we adopt a viewing angle of $\theta_{\rm obs} = 45°$, representing a line of sight inclined 45° to the z-axis in the simulation domain. A total of nine representative evolutionary stages after the year 1793 are selected for systematic radiative modelling and visualization.

As shown in Fig. 7 (Model C), in the year 1858, the surface brightness distribution of synchrotron radiation from the centrally free-expanding PWN is clearly visible. Its spatial extent is consistent with the density slice shown in Fig. 3, where the radiation region of the PWN extends along the equatorial plane to approximately 4 pc. The interaction between the PWN polar regions and the reverse shock of the SNR leads to magnetic field instabilities, resulting in weaker synchrotron emission in these regions at this stage. By the year 2673, following the full interaction between the PWN and the SNR, bright arc-like structures emerged at the poles. After further compression of the PWN by the SNR, the inner and outer rings similar to the Crab Nebula form in the central region in the year 3716. The pronounced contrast in radiation between the rings may arise from differences in magnetic field gradients and spatial variations in particle acceleration efficiency. Meanwhile, the high velocity of the pulsar causes a downstream ($-z$-axis) displacement of the central bright ring. During the re-expansion phase at year 4955, the central emission regions indicate strong radiation features associated with bipolar jets, while the outer spherical radiation shell gradually increases in brightness. This spherical emission is attributed to contributions from RTI-dominated regions formed by mixing tracked pulsar wind particles and the reverse shock of the SNR. The physical correlation is confirmed by the spatial scale comparison in year 6520 between Figs 5 ($P_{\rm mag}$ slice) and 7, where the outer radiation and $P_{\rm mag}$ boundaries are located at approximately 10 pc.

As illustrated in Fig. 8, under a higher ISM density of 0.5 cm^{-3}, the surface brightness distribution of synchrotron radiation in the X-ray band exhibits evolutionary features similar to those of Fig. 7. However, because of the significant influence of the dense ISM environment, the expansion dynamics contrasts with the low-density case: the enhanced hydrodynamic pressure of the high-density ISM strongly suppresses the free expansion of the PWN. Consequently, the intensity of the centra radiation region increases by approximately three orders of magnitude compared to Model C. With the continued enhancement of reverse shock interactions, by the year 3716, the anisotropic compression from the shock becomes the dominant factor shaping the PWN evolution, resulting in a directionally selective, cone-shaped radiation structure. Eventually, by year 6259, the system exhibits segmented radiation patterns, where the ring-like structures split into discrete emission patches along the direction of motion.

4 DISCUSSION

4.1 The influence of the progenitor wind environment

This study adopts a simplified model in which supernova ejecta expand into a uniform ISM. Admittedly, the assumption of a uniform ISM represents a considerable simplification of the authentic astrophysical environment. In a realistic physical picture, the stellar wind from the progenitor star plays a pivotal role throughout its evolution. In this context, an extensive body of work has been conducted by Meyer et al. (2014, 2020, 2021, 2024) and Meyer & Meliani (2022). Their research reveals that the complex and asymmetric structures of the CSM, which are presculpted by the wind activities of massive progenitors, particularly runaway stars, exert a decisive, and often dominant, influence on the subsequent evolution of the PWN.

In the model presented by Meyer et al. (2020), the interaction of the supernova shock with the dense bow shock, sculpted by the progenitor's stellar wind ahead of its motion, results in a highly anisotropic expansion of the SNR. Energy is preferentially channelled into the lower density wake region. This global asymmetry, dictated by the CSM, is subsequently imparted to the interior PWN, causing it to assume an ovoidal shape morphology with persistent equatorial asymmetries. The collision of the supernova forward shock with dense shells within the CSM (WR rings or RSG wind shells) generates a strong reverse shock. This shock propagates inward, drastically compressing the PWN, and potentially triggering a reverberation of its termination shock (Bandiera et al. 2023a, b; Meyer et al. 2024). In such environment-dominated scenarios, the PWN morphology can be distorted from the classical cross-like structure of Komissarov & Lyubarsky (2004) into a gyroscope-like or even more intricate configuration. Thus, its geometry is determined more by the pre-existing structure of the CSM than by the intrinsic motion of the pulsar.

In contrast, the uniform medium model adopted in this study provides a relatively quiescent environment for the evolution of the PWN, as it is devoid of the strong reverse shock driven by the CSM. Consequently, the morphological evolution observed in our model – such as the formation of the bow shock and the elongation of the tail – can be unambiguously attributed to the dominant effect of the pulsar's high-velocity motion. This constitutes the central contribution of our research. It should be noted that the aforementioned studies emphasizing the importance of CSM, such as those by Meyer et al. (2020), often neglect the pulsar kick velocity in their models to effectively isolate the CSM effects. Therefore, their conclusions are mainly applicable to the low-velocity pulsar population, which represents approximately 2–5 per cent of the total population (Igoshev 2020). Our research, on the contrary, focuses on a more astrophysically prevalent scenario: a pulsar endowed with a typical high kick velocity (Verbunt et al. 2017). As such, our model and the CSM-dominated models are not mutually exclusive; instead, they represent two complementary physical scenarios crucial for understanding the morphological diversity of PWNe. This study provides an indispensable baseline model for quantitatively assessing the relative importance of the CSM reverberation driven by the environment versus the pulsar kick-driven dynamics within realistic astrophysical settings.

Furthermore, from the perspective of observable synchrotron characteristics, the results of our simulations are consistent with specific progenitor evolutionary models. In models that incorporate a complex CSM, the type of progenitor significantly impacts the observable features. For example, simulations featuring a WR star as progenitor (Meyer et al. 2021, 2024) indicate that the bright shell produced by the SNR–CSM interaction can completely obscure the central PWN. In contrast, for simulations with the RSG progenitor, the central structures, such as the PWN jet, emerge as the brightest regions of emission because of the lower density of the surrounding wind bubble. Our simulation results, as shown in Figs 7 and 8, clearly exhibit a bright central PWN structure that is not concealed by the outer shell. This feature is in better agreement with the predictions for the RSG progenitor model. Given that RSGs are one of the most common types of core-collapse supernova progenitors for massive stars (Katsuda et al. 2018), and form relatively low-density wind bubbles, the reverse shock of the resulting SNR is less influenced by the reverberation effect from the external CSM. Therefore, for the purpose of simulating pulsar systems that originate from RSGs and possess high kick velocities, our assumption of a uniform ISM serves as an effective and representative approximation for capturing the key physical processes dominated by the pulsar's motion.

4.2 Limitations of the simulation model

As mentioned in Section 3.2, the absence of a bow shock structure at the end of the simulation can be mainly attributed to two limitations in our model set-up. First, our simulation employs a high magnetization parameter (σ) within an axisymmetric framework, which promotes the formation of a collimated jet structure in the polar regions of the pulsar wind (Del Zanna et al. 2004). Since the pulsar is set to move along the z-axis (coinciding with the jet direction), its velocity (approximately 500 km s^{-1}) is substantially lower than that of the relativistic jet. Consequently, it is difficult for a distinct bow shock structure to form along the z-axis throughout the simulation. On the other hand, the time-scale $t_{\rm cr}$ for a pulsar to escape its SNR is given by van der Swaluw et al. (2003) as

$$t_{\rm cr} \approx 1.4 \times 10^4 E_{51}^{1/3} V_{\rm psr}^{-5/3} n^{-1/3}\ {\rm yr}. \quad (18)$$

Furthermore, the study by van der Swaluw et al. (2004) indicates that for a bow shock to be observable, the pulsar Mach number must reach unity, which corresponds to a simulation time of at least $t = 0.5t_{\rm cr}$. Therefore, within our simulation's duration, it is challenging to produce a discernible bow shock structure, regardless of whether the magnetization parameter is lowered or the pulsar's direction of motion is altered. To observe such a structure, based on the expression for $t_{\rm cr}$, Model C would need to evolve for at least 95 700 yr, while Model D would require at least 56 000 yr. Given our current grid resolution, computational domain size, and available computational resources, achieving such a long-term evolution remains computationally challenging.

The numerical methodology employed in this study is constructed within a 2D framework. Although this approach substantially reduces computational complexity, it inherently suppresses the degrees of freedom for non-axisymmetric evolution that exist in 3D space. This geometric constraint imposes axisymmetry upon the system, thereby precluding the development of non-axisymmetric instabilities that are crucial in realistic 3D environments. For example, structures such as the z-pinch, which can be sustained in 2D models, are rapidly disrupted in 3D by the growth of the kink instability (Mizuno et al. 2011). Consequently, 2D simulations tend to produce polar jets that are overly collimated and artificially strong. More realistic 3D studies suggest that such features may be numerical artefacts, as the jets would lose their collimation and coherence due to these instabilities in practice. Consequently, the elongation of the nebula along the jet axis predicted by the z-pinch effect (e.g. as interpreted by Begelman & Li 1992) is not observed in more realistic 3D simulations, where the morphology instead remains

very spherical. More importantly, 2D models cannot capture the processes of magnetic field randomization and internal magnetic dissipation driven by 3D turbulence and kink instabilities. This process is considered key to resolving the σ paradox, as it efficiently converts magnetic energy into particle energy within the nebula, thus reconciling the high σ pulsar wind with the observed low-magnetization nebula (Komissarov 2013).

In addition to the inherent physical biases introduced by the 2D geometric simplification, our simulations omit several other key physical factors. These include the misalignment angle between the pulsar's spin and magnetic axes, the multidimensional nature of the pulsar's proper motion, and the realistic density distribution of the ISM. The model assumes a constant spin-down luminosity for the pulsar, with a fixed initial period, period derivative, and wind magnetization parameter. In reality, however, a pulsar's spin period increases with age, which in turn modifies the spin-down luminosity, leading to deviations between the simulated evolution and the actual behaviour.

Additionally, in the reconstruction of the synchrotron surface brightness, the model assumes a power-law energy distribution for electrons. This approach neglects relativistic effects such as Doppler frequency shifts in the radiation field (Del Zanna et al. 2006; Volpi et al. 2008) and does not solve the full radiative transfer equation. Furthermore, since the computational domain is defined in spherical (or spherical shell) coordinates, visualization using tools such as YT requires interpolation onto a Cartesian grid, a process that can introduce image data artefacts or interpolation errors.

Aforementioned spatial complexities and intricate physical processes, which are suppressed in our 2D axisymmetric simulations, motivate the need for 3D investigations. Consequently, a 3D approach is expected to provide a more comprehensive understanding of various complex phenomena, such as the helical instabilities of the toroidal magnetic field, anisotropic shock structures, and 3D turbulent dissipation mechanisms. However, such studies are computationally expensive and significantly more time-consuming.

4.3 Comparison with particular PWNe

Several young subsonic pulsars generate PWNe that exhibit relatively weak toroidal structures in X-ray images obtained by the *Chandra* Advanced CCD Imaging Spectrometer, such as in the cases of Kes 75 and MSH 15−52 (cf. fig. 3 in Kargaltsev et al. 2017). Our numerical simulations reveal that such objects tend to develop quasi-spherical geometries along the pulsar's direction of motion during their early evolutionary stages (see Figs 7 and 8). Notably, their radiation properties display pronounced spatial segmentation: the head and tail regions of the PWN exhibit a distinct decoupling in radiation intensity. This observational feature shows strong agreement with the simulated synchrotron radiation intensity maps presented in this study, particularly in the evolutionary stages of 5737 and 6259 yr (see Fig. 8).

The G327.1−1.1 (Snail) PWN, which harbours an undetected pulsar, exhibits a distinct radio morphology. Its tail maintains a constant surface brightness over a length of 1.5 arcmin before terminating in a spherical feature. This configuration strongly indicates that the PWN is confined within its host SNR, and the spherical structure is likely the reverse shock of the SNR (Ma et al. 2016). This scenario is supported by the predicted pulsar velocity of 500 km s^{-1} derived from the Australia Telescope National Facility Pulsar Catalogue (Manchester et al. 2005), a value that matches the parameters of our simulation and is consistent with the PWN not having escaped the SNR. Moreover, the observed radio morphology of the Snail (cf. fig. 7 in Kargaltsev et al. 2017) is in agreement with the density structure of our simulation in $t = 5738$ yr (Fig. 3), specifically within the spatial slice of $-8 \leq Z \leq 1$ pc and $0 \leq R \leq 4$ pc.

5 CONCLUSION

The high-resolution 2.5D axisymmetric RMHD model developed in this study successfully captures the main dynamical processes governing the early evolutionary stages of composite PWN–SNR systems, specifically under the influence of pulsar spatial motion and varying ISM densities. In particular, when a representative pulsar kick velocity of approximately 500 km s^{-1} is adopted, the simulations reveal a pronounced eccentric evolution of the PWN, accompanied by significant morphological asymmetries, alterations in the magnetic field configuration, and shifts in the distribution of synchrotron-emitting regions. These results closely match a range of observational findings, lending strong support to the physical plausibility and effectiveness of the adopted velocity and density parameters.

In high-density ISM environments, increased external confinement and improved compression efficiency drive the PWN into a non-linear evolutionary regime at a relatively early stage. In this scenario, interaction with the SNR reverse shock occurs significantly sooner, leading to a markedly shortened compression phase and a conspicuous restriction on the forward shock expansion. During this compression phase, the synchrotron-bright region becomes more compact and luminous, and the magnetic field structure is further tightened. However, in the subsequent re-expansion stage, the emitting zones become fragmented, forming segmented radiative regions that manifest as distinct observational features.

In contrast, in low-density ISM environments, the PWN encounters the reverse shock at later times. Here, the compression phase proceeds more gradually and is characterized by the emergence of jet-like features, which are absent in the high-density regime. This is consistent with previous 2D simulations (Del Zanna et al. 2004), which show that increased wind magnetization promotes polar jet formation through magnetic hoop stresses. However, our findings indicate that, following the PWN and SNR reverse shock interaction, the persistence and morphology of the jets are no longer solely determined by σ but are instead closely linked to the ambient density of the ISM and possibly other complex interdependent factors.

Although this study presents high-resolution, system-scale simulations within a 2D framework and effectively reconstructs 3D radiative properties using 2.5D techniques, the inherent axisymmetry of the model precludes the development of fully 3D asymmetries. Furthermore, the adoption of idealized initial parameters limits the general applicability of our results to later evolutionary stages. Future work aimed at capturing the complex and diverse evolution of PWN–SNR systems will necessitate fully 3D MHD simulations coupled with dynamically evolving pulsar models. Key advancements will include the implementation of realistic 3D pulsar trajectories and arbitrarily oriented magnetic axes, which are essential for simulating the more general and observationally comparable morphologies of PWNe.

ACKNOWLEDGEMENTS

This work was supported by the National Natural Science Foundation of China (grant numbers 12393852 and 12563010), Yunnan Fundamental Research Projects (grant number 202501AS070068), the Scientific Research Fund of the Yunnan Provincial Department

of Education, and the Graduate Research Innovation Fund of Yunnan University (grant number KC-24249493).

DATA AVAILABILITY

The results presented in this paper were generated using the publicly available ATHENA++ MHD code (Stone et al. 2020). The specific problem generator, input files, and the raw simulation data underlying this article will be shared on reasonable request with the corresponding author.

REFERENCES

Bandiera R., Bucciantini N., Martín J., Olmi B., Torres D. F., 2023a, MNRAS, 520, 2451
Bandiera R., Bucciantini N., Olmi B., Torres D. F., 2023b, MNRAS, 525, 2839
Barkov M. V., Lyutikov M., Khangulyan D., 2019, MNRAS, 484, 4760
Begelman M. C., Li Z.-Y., 1992, ApJ, 397, 187
Blondin J. M., Chevalier R. A., Frierson D. M., 2001, ApJ, 563, 806
Bogovalov S., Khangoulyan D., 2002, Astron. Lett., 28, 373
Bucciantini N., 2002, A&A, 387, 1066
Bucciantini N., 2018, MNRAS, 478, 2074
Bucciantini N., Amato E., Bandiera R., Blondin J. M., Del Zanna L., 2004, A&A, 423, 253
Bucciantini N., Amato E., Del Zanna L., 2005, A&A, 434, 189
Camilo F., Gaensler B. M., Gotthelf E. V., Halpern J. P., Manchester R. N., 2004, ApJ, 616, 1118
Camus N., Komissarov S., Bucciantini N., Hughes P., 2009, MNRAS, 400, 1241
Cao Z. et al., 2024, Radiat. Detect. Technol. Methods, 8, 1437
Coroniti F., 1990, ApJ, 349, 538
Del Zanna L., Amato E., Bucciantini N., 2004, A&A, 421, 1063
Del Zanna L., Volpi D., Amato E., Bucciantini N., 2006, A&A, 453, 621
Gaensler B. M., Arons J., Kaspi V. M., Pivovaroff M. J., Kawai N., Tamura K., 2002, ApJ, 569, 878
Gaensler B. M., Slane P. O., 2006, ARA&A, 44, 17
Helfand D. J., Gotthelf E. V., Halpern J. P., 2001, ApJ, 556, 380
Hester J. J. et al., 2002, ApJ, 577, L49
Hester J. J., 2008, ARA&A, 46, 127
Igoshev A. P., 2020, MNRAS, 494, 3663
Jun B.-I., Norman M. L., 1996, ApJ, 472, 245
Kargaltsev O., Pavlov G. G., Klingler N., Rangelov B., 2017, J. Plasma Phys., 83, 635830501
Katsuda S., Takiwaki T., Tominaga N., Moriya T. J., Nakamura K., 2018, ApJ, 863, 127
Kennel C. F., Coroniti F. V., 1984, ApJ, 283, 694
Komissarov S. S., 2013, MNRAS, 428, 2459
Komissarov S. S., Lyubarsky Y. E., 2003, MNRAS, 344, L93
Komissarov S. S., Lyubarsky Y. E., 2004, MNRAS, 349, 779
Lu F. J., Wang Q. D., Aschenbach B., Durouchoux P., Song L. M., 2002, ApJ, 568, L49
Lyubarsky Y. E., 2002, MNRAS, 329, L34
Ma Y. K., Ng C. Y., Bucciantini N., Slane P. O., Gaensler B. M., Temim T., 2016, ApJ, 820, 100
Manchester R. N., Hobbs G. B., Teoh A., Hobbs M., 2005, AJ, 129, 1993
Meyer D. M. A., Mackey J., Langer N., Gvaramadze V. V., Mignone A., Izzard R. G., Kaper L., 2014, MNRAS, 444, 2754
Meyer D. M. A., Meliani Z., 2022, MNRAS, 515, L29
Meyer D. M. A., Meliani Z., Torres D. F., 2024, A&A, 692, A207
Meyer D. M. A., Petrov M., Pohl M., 2020, MNRAS, 493, 3548
Meyer D. M. A., Torres D. F., Meliani Z., 2025, A&A, 696, L9
Meyer D. M., Pohl M., Petrov M., Oskinova L., 2021, MNRAS, 502, 5340
Michel F. C., 1973, ApJ, 180, L133
Mizuno Y., Lyubarsky Y., Nishikawa K.-I., Hardee P. E., 2011, ApJ, 728, 90
Olmi B., Bucciantini N., 2019, MNRAS, 484, 5755
Olmi B., Bucciantini N., Morlino G., 2018, MNRAS, 481, 3394
Olmi B., Del Zanna L., Amato E., Bandiera R., Bucciantini N., 2014, MNRAS, 438, 1518
Olmi B., Del Zanna L., Amato E., Bucciantini N., Mignone A., 2016, J. Plasma Phys., 82, 635820601
Pavan L. et al., 2016, A&A, 591, A91
Porth O., Komissarov S. S., Keppens R., 2013, MNRAS, 431, L48
Porth O., Komissarov S. S., Keppens R., 2014, MNRAS, 438, 278
Romani R. W., Ng C. Y., 2003, ApJ, 585, L41
Romani R. W., Ng C. Y., Dodson R., Brisken W., 2005, ApJ, 631, 480
Slane P., Helfand D. J., van der Swaluw E., Murray S. S., 2004, Am. Astron. Soc. HEAD Meeting, #8, 08.01
Stone J. M., Tomida K., White C. J., Felker K. G., 2020, ApJS, 249, 4
Temim T., Slane P., Kolb C., Blondin J., Hughes J. P., Bucciantini N., 2015, ApJ, 808, 100
Temim T., Slane P., Plucinsky P. P., Gelfand J., Castro D., Kolb C., 2017, ApJ, 851, 128
Toropina O. D., Romanova M. M., Lovelace R. V. E., 2019, MNRAS, 484, 1475
Toropina O. D., Romanova M. M., Toropin Y. M., Lovelace R. V. E., 2001, ApJ, 561, 964
Turk M. J., Smith B. D., Oishi J. S., Skory S., Skillman S. W., Abel T., Norman M. L., 2011, ApJS, 192, 9
van der Swaluw E., Achterberg A., Gallant Y. A., Downes T. P., Keppens R., 2003, A&A, 397, 913
van der Swaluw E., Downes T. P., Keegan R., 2004, A&A, 420, 937
Verbunt F., Igoshev A., Cator E., 2017, A&A, 608, A57
Vigelius M., Melatos A., Chatterjee S., Gaensler B., Ghavamian P., 2007, MNRAS, 374, 793
Volpi D., Del Zanna L., Amato E., Bucciantini N., 2008, A&A, 485, 337
Wilkin F. P., 1996, ApJ, 459, L31
Wu K., Zhou L., Gong Y., Fang J., 2023, MNRAS, 519, 1881
Xia Q., Wang H.-Y., Xian Y.-J., Fang J., 2025, Res. Astron. Astrophys., 25, 085006
Zhou L., Wu K., Gong Y., Fang J., 2024, MNRAS, 529, 3593
Zhu B.-T., Zhang L., Fang J., 2018, A&A, 609, A110

This paper has been typeset from a TEX/LATEX file prepared by the author.